ISSN 0915-633X

NATIONAL INSTITUTE FOR FUSION SCIENCE

A Nondissipative Simulation Method for the Drift Kinetic Equation

T-H Watanabe, H. Sugama and T. Sato

(Received - June 8, 2001)

NIFS-707 July 2001

RESEARCH REPORT
NIFS Series

TOKI, JAPAN

A nondissipative simulation method for the drift kinetic equation

Tomo-Hiko WATANABE, Hideo SUGAMA, and Tetsuya SATO

National Institute for Fusion Science / Graduate University for Advanced Studies, Toki, Gifu, 509-5292

(Received June 8, 2001)

With the aim to study the ion temperature gradient (ITG) driven turbulence, a nondissipative kinetic simulation scheme is developed and comprehensively benchmarked. The new simulation method preserving the time-reversibility of basic kinetic equations can successfully reproduce the analytical solutions of asymmetric three-mode ITG equations which are extended to provide a more general reference for benchmarking than the previous work [T.-H. Watanabe, H. Sugama, and T. Sato: Phys. Plasmas 7 (2000) 984]. It is also applied to a dissipative three-mode system, and shows a good agreement with the analytical solution. The nondissipative simulation result of the ITG turbulence accurately satisfies the entropy balance equation. Usefulness of the nondissipative method for the drift kinetic simulations is confirmed in comparisons with other dissipative schemes.

KEYWORDS: drift wave, drift kinetics, gyrokinetics, computer simulation

§1. Introduction

It is considered that the ion temperature gradient (ITG) driven turbulence plays an important role in causing the anomalous ion heat transport in a core of tokamaks.[1] In order to study the transport mechanism and predict the thermal diffusivity, a lot of efforts have been devoted to development of numerical simulation methods of the ITG turbulence. The three-mode coupling system[2] for the slab ITG mode[3] in a two-dimensional configuration is employed for benchmarking of gyrokinetic, gyrofluid and drift-kinetic-Vlasov simulation codes as well as kinetic fluid closure models.[4–7] Recently, we have derived a class of exact solutions of the three-mode ITG problem, which is written in terms of the eigenfunctions of the linear unstable mode and the Jacobi's elliptic functions of the time.[6] The analytical solution gives a useful reference for basic benchmarking of various theories and simulations for the ITG turbulence. In our previous work,[6] it is also confirmed that the nondissipative drift-kinetic-Vlasov simulation code with the implicit midpoint time-integration can successfully reproduce the exact solutions of the three-mode ITG equations. However, no direct comparison with other time-integration methods was made in the benchmark test which was also limited to a collisionless three-mode system with the symmetry condition of $(1,1)$ and $(-1,1)$ modes of the ion distribution function [where (m,n) denote mode numbers in the antiparallel directions to a pressure gradient and the diamagnetic drift of ions].

In the Vlasov simulation (in our terminology, it is called Boltzmann simulation, when a finite collisionality is introduced), time-evolution of the distribution function is directly calculated in the phase space (or its Fourier space), while the particle-based simulations follow trajectories of super particles (or markers) according to their equations of motions. The predictor-corrector scheme is often employed for time-integration of the drift kinetic (or gyrokinetic) equation in both of the Vlasov[5,8,9] and particle simulations.[10,11] Comparisons of results from different numerical schemes with each other would contribute to verifying their applicability.

It is widely believed that stabilization by a shear (zonal) flow is one of key mechanisms in saturation of the ITG turbulence.[12] Even in a regime where the ITG instability is collisionless, it is considered that a finite collisionality plays an important role in decay of the shear flow and in the consequent enhancement of the transport.[13] Thus, benchmark tests of simulation code should be extended to take into account effects of the shear flow and the finite collisionality

In this paper, we report results of comprehensive benchmark tests of the nondissipative drift-kinetic-Vlasov simulation method. The paper is organized as follows. In §2.1, we consider simulation methods for the Vlasov-Poisson system, and generalize the splitting scheme[14] into higher-orders by applying the symplectic integrator.[15,16] This provides an outlook for developing the nondissipative drift kinetic simulation scheme which is described in §2.2. In §3, we show results of benchmark tests for dissipative and asymmetric three-mode problems of which analytical solutions are derived in Appendixes A-D, where a simple example of stabilization by an external shear flow is described. We also compare the results with those of other time-integration methods, such as the predictor-corrector and the Runge-Kutta-Gill methods. The nondissipative scheme is applied to the slab ITG turbulence in §4, where we specifically focus on the entropy balance[7] and a convergence check for the velocity space resolution. Finally, we summarize the results in §5.

§2. Basic schemes

2.1 Vlasov-Poisson system

We start with investigation of numerical algorithms for a simpler equation which has common features as the

drift kinetic and gyrokinetic equations. It would provide an insight into development of simulation schemes for drift waves. The one-dimensional Vlasov-Poisson system is a good example for our purpose. Various methods for numerically solving the Vlasov-Poisson equations of

$$\frac{\partial f}{\partial t} + v\frac{\partial f}{\partial x} + \frac{\partial \phi}{\partial x}\frac{\partial f}{\partial v} = 0 \tag{2.1}$$

and

$$-\frac{\partial^2 \phi}{\partial x^2} = 1 - \int f dv \tag{2.2}$$

had been extensively developed in 1970's to study nonlinear kinetic phenomena in electrostatic plasmas. Here, f and ϕ mean the electron distribution function and the electrostatic potential, respectively. Equations (2.1) and (2.2) are normalized by $x = x'/\lambda_D$, $t = t'\omega_p$, $v = v'/v_t$, $f = f' v_t/n_0$, $\phi = e\phi'/m_e v_t^2$, where prime means dimensional quantities; e, m_e, and n_0 are the elementary charge, the electron mass, and the average density. λ_D and ω_p, respectively, denote the Debye length and the plasma frequency of which product gives the thermal velocity $v_t = \lambda_D \omega_p$. Background immobile ions are also assumed.

One of the Vlasov simulation methods which is nondissipative and preserves the time-reversibility of eq.(2.1) is the splitting scheme proposed by Cheng and Knorr[14] with the Fourier mode interpolation.[17] In the splitting scheme, a time-integration procedure of the Vlasov equation is separated into three steps,

$$\begin{cases} f^*(x,v) = f^n(x - v\Delta t/2, v) \\ f^{**}(x,v) = f^*(x, v - \Delta t \partial\phi/\partial x) \\ f^{n+1}(x,v) = f^{**}(x - v\Delta t/2, v) \end{cases} . \tag{2.3}$$

The coordinate transformation of $x - v\Delta t/2$ can be accurately calculated in the Fourier space by multiplying a phase shifting factor of $\exp(-ikv\Delta t/2)$. Similarly, the transformation of $v - \Delta t \partial\phi/\partial x$ is carried out in the velocity wave number space by multiplying $\exp(-i\ell\Delta t \partial\phi/\partial x)$. Here, ℓ denotes a wave number in the velocity space. When $k \ll \pi/\Delta x$ and $\ell \ll \pi/\Delta v$, the distribution function f, which is a constant of particle motion, is well preserved along the characteristics of the Vlasov equation (a particle trajectory). In other words, f is just advected in the x (v) space by eq.(2.3) with the velocity v (the acceleration $\partial\phi/\partial x$) which is independent of x (v).

From a point of view of a particle motion, the splitting scheme is related to the leap-frog integrator,

$$\begin{cases} x^* = x^n + v^n \Delta t/2 \\ v^* = v^n + \Delta t \frac{\partial \phi}{\partial x}(x^*) \\ x^{n+1} = x^* + v^* \Delta t/2 \\ v^{n+1} = v^* \end{cases} \tag{2.4}$$

which is often used in particle simulations[18] of the Vlasov-Poisson system in terms of the equivalent form of

$$\begin{cases} v^{n+\frac{1}{2}} = v^{n-\frac{1}{2}} + \Delta t \frac{\partial \phi}{\partial x}(x^n) \\ x^{n+1} = x^n + v^{n+\frac{1}{2}} \Delta t \end{cases} . \tag{2.5}$$

It has the second-order accuracy in time and keeps the time-reversibility. We note that the leap-frog method is identical to one of the second-order symplectic integrators which preserve a symplectic 2-form of a Hamiltonian system. The explicit symplectic integrator for a Hamiltonian system of $dz/dt = \{z, H\}$, where $\{,\}$ denotes the Poisson brackets, is constructed as follows.[15,16] The Hamiltonian is assumed to be separable for the canonical coordinates $z = (q,p)$, that is, $H(q,p) = T(p) + V(q)$. A formal solution of the Hamilton's equation is

$$z(t) = \left[\exp\left(\int_0^t (D_T + D_V) dt\right)\right] z(0) , \tag{2.6}$$

where differential operators, D_T and D_V, are $[\partial T(p)/\partial p]\,\partial/\partial q$ and $-[\partial V(q)/\partial q]\,\partial/\partial p$, respectively. For discretized time, the formal solution gives

$$z^{n+1} = \prod_{i=1}^{k} \exp(d_i \Delta t D_V) \exp(c_i \Delta t D_T) z^n . \tag{2.7}$$

Expansion of the exp operators leads to succession of symplectic mappings,

$$\begin{cases} q_i = q_{i-1} + c_i \Delta t \frac{\partial T}{\partial p}(p_{i-1}) \\ p_i = p_{i-1} - d_i \Delta t \frac{\partial V}{\partial q}(q_i) \end{cases} \quad \text{for } i = 1, 2, ..., k , \tag{2.8}$$

where one can choose k, c_i, and d_i so that eq.(2.8) has any order of accuracy. For the second-order accuracy, the simplest set of $k = 2$, $c_1 = c_2 = 1/2$, $d_1 = 1$, and $d_2 = 0$ gives the leapfrog scheme in eq.(2.4). The following set has been derived for the fourth-order ($k = 4$) symplectic integrator,[15]

$$\begin{aligned} &c_1 = c_4 = \frac{1}{2(2 - 2^{1/3})}, \qquad c_2 = c_3 = \frac{1 - 2^{1/3}}{2(2 - 2^{1/3})}, \\ &d_1 = d_3 = \frac{1}{2 - 2^{1/3}}, \qquad d_2 = -\frac{2^{1/3}}{2 - 2^{1/3}}, \qquad d_4 = 0. \end{aligned} \tag{2.9}$$

Coefficients for the sixth-order methods have also been obtained.[16]

Here, we note that the splitting scheme solving the Vlasov equation, $\partial f/\partial t = -\{f, H\}$, is regarded as a mapping generated by the leapfrog integrator. Thus, extension of the splitting scheme into higher-orders is achieved by applying a higher-order symplectic integrator to coordinate transformations in the mapping. The higher-order simulation scheme for the Vlasov equation is written as

$$\begin{cases} f_i^*(q,p) = f_{i-1}(q - c_i \Delta t \partial T/\partial p, p) \\ f_i(q,p) = f_i^*(q, p + d_i \Delta t \partial V/\partial q) \end{cases} \quad \text{for } i = 1, 2, ..., k , \tag{2.10}$$

which is a mapping of f generated by the symplectic integrator. Here, $V(q)$ in the argument of f_i^* is given by solving the Poisson's equation in which $f_i^*(q,p)$ is used. Equations (2.9) and (2.10) construct the fourth-order simulation scheme of the Vlasov-Poisson system, which is generalization of the splitting scheme.

Figure 1 shows fluctuations of the total energy $\mathcal{E} = \frac{1}{2}[\int v^2 f dx dv + \int (\partial\phi/\partial x)^2 dx]$ in simulations with the second and fourth-order schemes, where the nonlinear Landau damping is examined for the initial condition of $f(x,v,t=0) = F_M(v)(1 + A\cos kx)$. $F_M(v)$ denotes the Maxwellian, $F_M(v) = \exp(-v^2/2v_t^2)/\sqrt{2\pi}v_t$. Used

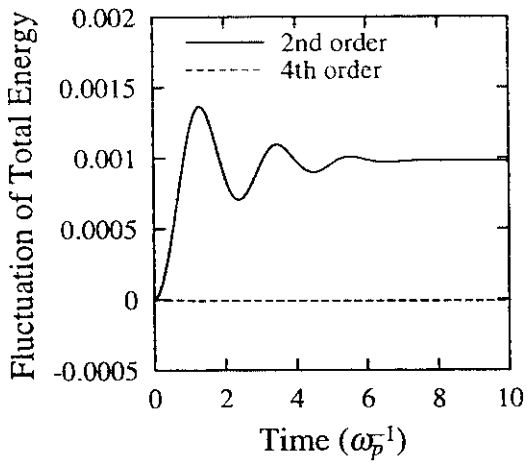

Fig. 1 Comparison of second- and fourth-order schemes

parameters are $A = 0.5$, $k = 0.5\lambda_D^{-1} = 2\pi/L$, $L = 64\Delta x$, $-10v_t \le v \le 10v_t$, $\Delta v = 10v_t/512$, and $\Delta t = \omega_p^{-1}/8$. It is expected that the simulation scheme in eq.(2.10) has a good conservation property of the total energy, since the time-reversible scheme is free from a secular error. Actually, even in the second-order case, fluctuating energy is less than 0.15% of the initial value, and shows no secular increase nor decrease. Conservation of the total energy is largely improved by using the fourth-order scheme as shown in Fig.1, which suggests that application of the symplectic integrator is suitable for time-integration of the Vlasov equation. In the next subsection, we consider a simulation scheme for the collisionless drift kinetic and gyrokinetic equations.

2.2 Drift kinetic system

Here, we consider the collisionless drift kinetic system in a slab geometry with a uniform magnetic field,

$$\frac{\partial f}{\partial t} + v_\parallel \nabla_\parallel f + \boldsymbol{v}_{E\times B}\cdot\nabla f + \frac{q}{m}E_\parallel \frac{\partial f}{\partial v_\parallel} = 0 \ , \qquad (2.11)$$

where $\boldsymbol{v}_{E\times B} = \boldsymbol{E}\times\boldsymbol{B}/B^2$. In the electrostatic and low-frequency limit, $\boldsymbol{E} = -\nabla\phi$ is usually given by the quasi-neutrality condition with the adiabatic electron response

$$\int f dv_\parallel = n_0\left[1 + \frac{e\left(\phi - \langle\phi\rangle\right)}{T_e}\right] \ , \qquad (2.12)$$

for the ion distribution function f (which is averaged in the perpendicular velocity space), the average density n_0, and the electron temperature T_e, where $\langle\phi\rangle$ means a magnetic surface average of ϕ.

A discrete spectral representation and/or discretization on numerical grids in the phase space make eq.(2.11) a set of ordinary differential equations. In a vector form, it can be written as

$$\frac{d\boldsymbol{U}}{dt} = \boldsymbol{F}(\boldsymbol{U}) \ , \qquad (2.13)$$

where $\boldsymbol{U}$ and $\boldsymbol{F}$, respectively, denote a discretized form of f and a nonlinear operator on f that represents the second, third and fourth terms of eq.(2.11). We expect that the symplectic integrator should be successfully applied to the time integration of eq.(2.11), since it has the same features as the Vlasov equation. In contrast to the Vlasov-Poisson system, however, we can not employ the explicit symplectic method in eq.(2.8) for the drift kinetic case, since the Hamiltonian of a $E\times B$ drift particle, $H(x,y,z,v_\parallel) = mv_\parallel^2/2 + q\phi(x,y,z)$, is non-separable for the perpendicular coordinates x and y which are a conjugate pair and satisfy $dx/dt = -B^{-1}\partial\phi/\partial y$ and $dy/dt = B^{-1}\partial\phi/\partial x$ (the parallel coordinate z and momentum $mv_\parallel$ are also conjugate to each other). Thus, we use one of the simplest implicit symplectic integrator with the second-order accuracy, that is, the implicit midpoint rule,

$$\boldsymbol{U}^{n+1} - \boldsymbol{U}^n = \Delta t\boldsymbol{F}\left[(\boldsymbol{U}^{n+1} + \boldsymbol{U}^n)/2\right] \ . \qquad (2.14)$$

It is known that, when eq.(2.13) is the canonical equation for canonical coordinates $\boldsymbol{U}$, eq.(2.14) generates a canonical transform of $\boldsymbol{U}$.[19] Unlike eq.(2.10), eq.(2.14) applied to the discretized drift kinetic equation is, however, not a mapping of f generated by the symplectic integrator for the drift-particle motion. Nevertheless, it clearly preserves the time-reversibility.

For the drift kinetic equation, eq.(2.11), before discretization in the phase space, the time-integration scheme using the implicit midpoint rule satisfies the conservation law of f^2. One can easily confirm that the implicit midpoint rule gives

$$\left(f^{n+1}\right)^2 - \left(f^n\right)^2 = -\Delta t\left[\nabla_\parallel v_\parallel + \nabla\cdot\boldsymbol{v}_{E\times B} + \frac{\partial}{\partial v_\parallel}\frac{qE_\parallel}{m}\right]\left(\frac{f^{n+1}+f^n}{2}\right)^2 \ . \qquad (2.15)$$

In a system with the periodic boundary for the real space, thus, the integral $\int d^3x dv_\parallel f^2$ (where $f \to 0$ for $v_\parallel \to \pm\infty$) is conserved during the numerical time-integration. Therefore, the time-integration method in eq.(2.14) is nondissipative. This is the advantage of applying eq.(2.14) to the collisionless drift kinetic equation for a perturbed distribution function, since it enables a highly accurate calculation of the so-called entropy balance[7,20] as shown in §4.

A fourth-order version of the time-reversible scheme can also be easily implemented,[21]

$$\begin{cases} \boldsymbol{Y}_1 - \boldsymbol{U}^n = d_1\Delta t\boldsymbol{F}\left[(\boldsymbol{Y}_1 + \boldsymbol{U}^n)/2\right] \\ \boldsymbol{Y}_2 - \boldsymbol{Y}_1 = d_2\Delta t\boldsymbol{F}\left[(\boldsymbol{Y}_2 + \boldsymbol{Y}_1)/2\right] \\ \boldsymbol{U}^{n+1} - \boldsymbol{Y}_2 = d_3\Delta t\boldsymbol{F}\left[(\boldsymbol{U}^{n+1} + \boldsymbol{Y}_2)/2\right] \ , \end{cases} \qquad (2.16)$$

where d_1, d_2, and d_3 are given in eq.(2.9). Both of eq.(2.14) and each step in eq.(2.16) can be solved by iteration. Application to the gyrokinetic equation is straightforward. In the followings, we show results from several benchmark tests for the nondissipative drift kinetic simulation scheme with the implicit midpoint time-integrator in eq.(2.14).

§3. Benchmark tests for three-mode ITG problem

3.1 *A brief review*

In this subsection, we briefly review the three-mode ITG problem.[2,6] We start from the electrostatic drift kinetic equation in a slab geometry with a uniform magnetic field in the y-z plane,

$$\partial_t \tilde{f} + \Theta v \partial_y \tilde{f} - \left(\partial_y \phi \partial_x \tilde{f} - \partial_x \phi \partial_y \tilde{f}\right) = -\partial_y \phi \left[1 + (v^2 - 1)\eta_i/2 + \Theta v\right] F_M(v) \ , \quad (3.1)$$

where $\tilde{f}$ denotes a perturbed distribution function of ions. The system is assumed to be uniform in the z-direction. In this section and Appendix A, v denotes the parallel velocity $v_\parallel$ for simplicity. The background density and temperature gradients that are constant with scale lengths of L_n and L_T in the x-direction are written as the first and second terms in the square brackets on the right hand side of eq.(3.1). The third term represents the Landau damping by the background ions. The above equation is normalized in the so-called gyrofluid units,[4] that is, $\tilde{f} = \tilde{f}' L_n v_{ti}/\rho_i n_0$, $x = x'/\rho_i$, $y = y'/\rho_i$, $v = v'/v_{ti}$, $t = t' v_{ti}/L_n$, $\eta_i = L_n/L_T$, and $\phi = e\phi' L_n/T_i \rho_i$. Prime means a dimensional quantity. Here, v_{ti}, ρ_i, n_0 and e are the ion thermal velocity, the ion gyro-radius, the background plasma density, and the elementary charge, respectively. The background ion temperature T_i ($= m_i v_{ti}^2$; m_i means the ion mass) is equal to the electron one T_e. Θ is defined as $\Theta = \theta L_n/\rho_i$ where an inclination of the magnetic field $\theta \ll 1$ is assumed. The adiabatic electron response and the quasi-neutrality condition give the perturbed potential $\phi - \langle\phi\rangle$,

$$\int \tilde{f} dv = \phi - \langle\phi\rangle \ . \quad (3.2)$$

Here, $\langle\cdots\rangle$ denotes average in the y-direction.

Employing the periodic boundary conditions in the x and y directions, $\tilde{f}$ and ϕ that are independent of z can be expanded in the Fourier series,

$$\tilde{f}(x,y,v,t) = \sum_{m,n} \tilde{f}_{m,n}(v,t) e^{i(k_x x + k_y y)} \ , \quad (3.3)$$

$$\phi(x,y,t) = \sum_{m,n} \phi_{m,n}(t) e^{i(k_x x + k_y y)} \ , \quad (3.4)$$

where $k_x = 2\pi m/L_x$ and $k_y = 2\pi n/L_y$ for $m = 0, \pm 1, \pm 2, \ldots$ and $n = 0, \pm 1, \pm 2, \ldots$ Here, we take $L_x = L_y$ of which L_x and L_y denote the system size in the x and y directions, respectively. For studying the three-mode coupling, we only keep $(m,n) = (\pm 1, \pm 1)$ and $(\pm 2, 0)$ modes with the reality conditions of $f_+ \equiv \tilde{f}_{1,1} = \tilde{f}^*_{-1,-1}$, $f_- \equiv \tilde{f}_{-1,1} = \tilde{f}^*_{1,-1}$ and $f_2 \equiv \tilde{f}_{2,0} = \tilde{f}^*_{-2,0}$. In a symmetric case studied in the previous works, $f_+ = f_- \equiv f_\pm$ and $\mathrm{Re}(\tilde{f}_{2,0}) = 0$ (thus, $\langle\phi\rangle = 0$) were also required.[2,6] Then, one arrives at the symmetric three-mode ITG equations that is obtained by substituting the symmetry condition into eqs.(A·1)-(A·6) in Appendix A where the asymmetric three-mode equations are derived.

The symmetric three-mode equations have a class of exact solutions written in terms of the real and imaginary parts of the eigenfunction, $f_{Lr}(v)$ and $f_{Li}(v)$, and the real eigenfrequency ω_r (see ref.6 or Appendix A), that is,

$$\begin{aligned} f_\pm(v,t) &= [a(t) f_{Lr}(v) + i b(t) f_{Li}(v)] \exp(-i\omega_r t), \\ f_2(v,t) &= i c(t) f_{Li}(v), \\ \phi(t) &= a(t) \exp(-i\omega_r t) \ . \end{aligned} \quad (3.5)$$

Here, $a(t)$, $b(t)$, and $c(t)$ are real-valued and obey the following ordinary differential equations,

$$\begin{aligned} da/dt &= \gamma b, \\ db/dt &= \gamma a - 2k^2 ac \ , \\ dc/dt &= 4k^2 ab \ . \end{aligned} \quad (3.6)$$

Equation (3.6) reduces to a Hamilton's equation with Hamiltonian of $H(a,b)$, and hence, turns out to be integrable.[7] The analytical solution (a,b,c) is given by the Jacobi's elliptic functions which are periodic in t. See ref.6 for more details of the analytical solution.

3.2 *Comparison with other methods*

The drift kinetic simulations with the implicit time-reversible integrators in eqs.(2.14) and (2.16) can accurately reproduce the analytical solution of the symmetric three-mode ITG equation.[6] Here, we compare the result with those of the predictor-corrector and the Runge-Kutta-Gill methods, which are second and fourth-order explicit schemes, respectively. The predictor-corrector method used here is written as,[10]

$$\begin{cases} \boldsymbol{U}^* = \boldsymbol{U}^{n-1} + 2\Delta t \boldsymbol{F}(\boldsymbol{U}^n) \\ \boldsymbol{U}^{n+1} = \boldsymbol{U}^n + \Delta t \boldsymbol{F}\left[(\boldsymbol{U}^* + \boldsymbol{U}^n)/2\right] \ , \end{cases} \quad (3.7)$$

which is known to be weakly dissipative.[11]

The initial condition is given by $f_\pm(v, t=0) = \varepsilon F_M(v)$ and $f_2(v, t=0) = 0$. The velocity space of $-5v_t \le v \le 5v_t$ is represented by 129 grid points. The time step is $\Delta t = 0.25$. Figure 2 shows the simulation results for $k = 0.1$, $\eta_i = 10$, $\Theta = 1$, and $\varepsilon = 10^{-5}$. For these parameters, the analytical solution predicts the period of $T = 353$. With respect to the linear growth rate and the first peak level of $|\phi|$, the three methods give the same results. After the peaking, $|\phi|$ decreases with the same rate as in the linear growth phase. In the case of the predictor-corrector method, however, the exponential decay stops at $|\phi| = 4.63 \times 10^{-2}$ due to the numerical dissipation, and then, the mode grows again. The periodic behavior of $|\phi|$ is lost by the predictor-corrector scheme. Thus, time interval of the first and second peaks of $|\phi|$ is shorter ($T = 143$) than a half of the period given by the analytical solution. Although the fourth-order Runge-Kutta-Gill method is less dissipative than the predictor-corrector, the periodic solution is not correctly reproduced. The minimum value of $|\phi|$ is 4.45×10^{-4}, and the interval of the first and second peaks is $T = 256$. The above comparison with the dissipative integrators highlights the success of the nondissipative schemes [eqs.(2.14) and (2.16)] in simulation of the symmetric three-mode ITG problem.

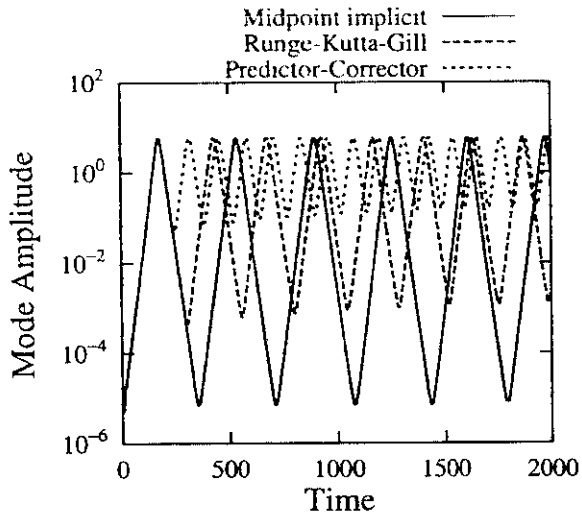

Fig. 2 Comparison of the implicit midpoint scheme with the predictor-corrector and the Runge-Kutta-Gill methods for $k = 0\,1$, $\eta_i = 10$, $\Theta = 1$, and $\varepsilon = 10^{-5}$

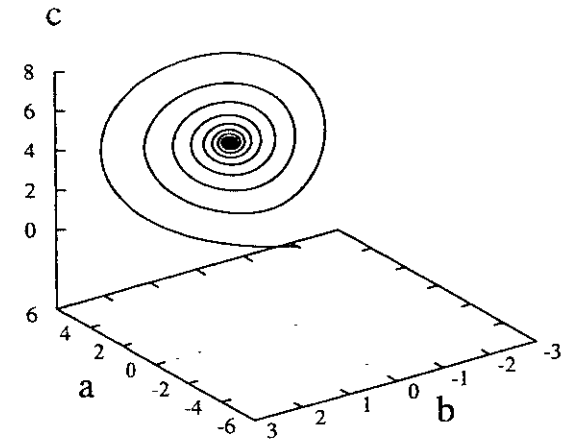

Fig. 3. Orbit in the (a, b, c)-phase space resulting from the drift kinetic simulation with the Krook collision term of $\nu = 10^{-2}$ Other parameters are the same as in Fig 2.

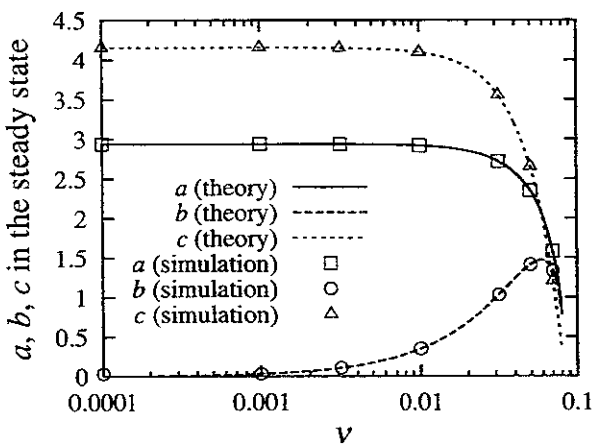

Fig. 4. Summary of a, b, and c in the steady state obtained by the drift kinetic simulations of the three-mode ITG problem with the Krook collision term for different values of ν (marks) Plotted lines show the stationary solution given by eq.(B3). Other parameters are the same as in Fig.2.

3.3 Dissipative three-mode ITG problem

If one compare the results of collisional and collisionless simulations, it is preferable to carry out the simulations using the same scheme that can be applicable to the both cases. Thus, we examine the applicability of the nondissipative scheme to a dissipative problem. In order to find out a reference of such benchmark tests, we have derived stationary solutions of the dissipative three-mode ITG problem with the Krook collision model in Appendix B.

We numerically solve the three-mode equations with the Krook collision term, $-\nu\tilde{f}$, on the right hand side, employing the implicit midpoint scheme. Even with the Krook collision term, the distribution functions of $(\pm 1, 1)$ and $(2, 0)$ modes resulting from the drift-kinetic-Boltzmann simulations are represented by the linear combination of $f_{Lr}(v)$ and $f_{Li}(v)$, since the three-mode equations can be reduced to the set of ordinary differential equations for (a, b, c) (see Appendix B). Time history of the simulation result for $\nu = 10^{-2}$ is plotted as an orbit in the (a, b, c)-phase space in Fig.3. The other parameters are the same as in Fig.2. One can see that the spiral orbit approaches to a fixed point. The final values of (a, b, c) for several different ν are summarized in Fig.4, where lines indicate the stationary solution given by eq.(B·3). The theoretical and numerical results show a good agreement, which confirms the applicability of the nondissipative simulation method to the dissipative three-mode ITG problem.

The dissipative integrators that fail to reproduce the periodic solutions of the collisionless three-mode ITG problem in the previous subsection would be sufficient for the case with the finite collisionality, if their numerical dissipation is negligiblly smaller than the physical one. It is, however, not trivial before running actual simulations. For comparison, we have also run the same simulations but with the predictor-corrector scheme, of which results for $\nu \geq 10^{-3}$ agree with the theoretical predictions. For the case of $\nu = 10^{-4}$, the value of a approaches 2.929 ($\equiv a_{\rm PC}$) in the predictor-corrector simulation, while the final value of $a = 2.939$ ($\equiv a_{\rm theory}$) is obtained by both of the theory and the nondissipative simulation in Fig.4. According to eq.(B·3), the effective dissipation $\nu_{\rm eff}$ is estimated as $(\nu_{\rm eff}/\gamma)^2 \simeq 1 - (a_{\rm PC}/a_{\rm theory})^2$, and thus, $\nu_{\rm eff} \sim 7 \times 10^{-3}$ (where $\gamma = 8.312 \times 10^{-2}$) for $\Delta t = 0.25$.

3.4 Asymmetric three-mode ITG problem

We have assumed the symmetry condition of $f_+ = f_-$ and $\mathrm{Re}(\tilde{f}_{2,0}) = 0$ in the above benchmark tests. In order to study interaction between turbulent eddies and a shear flow, however, one needs to take into account the $k_y = 0$ modes. Introduction of the shear flow component, $\phi_{2,0}$, into the three-mode equation breaks the symmetry of $(1, 1)$ and $(-1, 1)$ modes. For a case with a constant shear flow potential Φ, we perform benchmark tests for the asymmetric three-mode ITG problem of which fun-

damental properties are described in Appendix C.

In the earlier studies, we explicitly imposed the symmetry condition during the time-integration at every time step. Otherwise, asymmetry may grow from round-off errors, even if the symmetric initial condition is employed in computations. Actually, one finds symmetry breaking in the implicit midpoint simulation without imposing the symmetry condition (see Fig.5), where one of the modes continues to grow in the second period. The

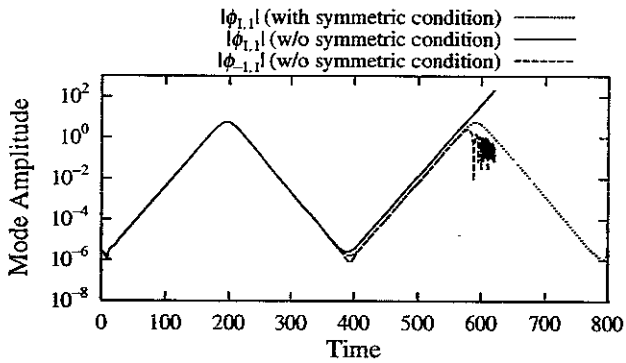

Fig. 5. Time-history of potential amplitudes of $(1,1)$ and $(-1,1)$ modes resulting from the drift kinetic simulation of the three-mode ITG problem without imposing the symmetry condition (solid and dashed lines). Dotted line indicates the symmetric result for comparison. The same parameters as in Fig.2 are used.

other one decays more slowly with a rapid oscillation which terminates the simulation at $t = 620$. Here, we employed the same parameters as in Fig.2. The above features are explained in the followings by analyzing the asymmetric three-mode equations given in Appendix A.

In order to consider the symmetry breaking found in Fig.5, we rewrite eq.(A·12) for $\Phi = 0$ by defining $\bar{a} \equiv \frac{1}{2}(a_+ + a_-)$, $\hat{a} \equiv \frac{1}{2}(a_+ - a_-)$, $\bar{b} \equiv \frac{1}{2}(b_+ + b_-)$, and $\hat{b} \equiv \frac{1}{2}(b_+ - b_-)$. If $\hat{a} = \hat{b} = 0$, $(\bar{a}, \bar{b}, c)$ satisfy the symmetric three-mode equation. Assuming $|\hat{a}|, |\hat{b}| \ll |\bar{a}|, |\bar{b}|, |c|$, we obtain a linearized equation for $\hat{a}$, which describes the linear stability of the symmetric solution, such that

$$\frac{d^2}{dt^2}\hat{a} = \gamma^2 \left[1 + \frac{2k^2}{\gamma} c(t)\right] \hat{a} \,. \tag{3.8}$$

Here, $c(t)$ is given by the symmetric solution which involves a quadratic term of the Jacobi's elliptic function of the time t.[6] Instead of analytically solving eq.(3.8), we discuss the stability qualitatively for the case that the symmetric solution $(\bar{a}, \bar{b}, c)$ starts from an initial condition with the small amplitude in the same way as in Fig.5. The orbit of the symmetric solution $(\bar{a}, \bar{b}, c)$ is close to the separatrix orbit $(a_{\rm sep}, b_{\rm sep}, c_{\rm sep})$ of

$$\begin{aligned} a_{\rm sep} &= \frac{\gamma}{\sqrt{2}k^2} \mathrm{sech}\left[\gamma(t - t_0)\right], \\ {b_{\rm sep}}^2 &= {a_{\rm sep}}^2 \left(1 - \frac{2k^4}{\gamma^2} {a_{\rm sep}}^2\right), \\ c_{\rm sep} &= \frac{2k^2}{\gamma} {a_{\rm sep}}^2 \end{aligned} \tag{3.9}$$

which emerges from (approaches to) the stationary point $(a_{\rm sep}, b_{\rm sep}, c_{\rm sep}) = (0, 0, 0)$. Here, t_0 denotes a constant. Thus, the maximum and minimum values of $c(t)$ are, respectively, $\max[c(t)] \simeq \gamma/k^2$ and $\min[c(t)] \sim O(\delta)$, where δ represents the order of the small initial amplitude. It is noteworthy that, for small δ, the linear growth and damping of $\bar{a}$ and $\bar{b}$ (where $|c(t)| \ll \max[c(t)]$) continue for a long time, while $|c(t)|$ can be as large as $\max[c(t)]$ only for a limited time of $O(\gamma^{-1})$. Contribution of $c(t)$ to the right hand side of eq.(3.8) is, thus, negligible in most of the period T of $(\bar{a}, \bar{b}, c)$, since $T \gg \gamma^{-1}$. Therefore, $\hat{a}$ is expected to grow with a rate $\simeq \gamma$. This means that the symmetric orbit is unstable to asymmetric perturbations in the linear growth and damping phases of the symmetric solution, and that the symmetry breaking found in Fig.5 occurs spontaneously.

After the symmetry breaking, one can see the predominant growth of the $(1,1)$ mode in Fig.5. This is explained in Appendix D by examining the linear stability of the exponentially growing solution with no external shear flow potential ($\Phi = 0$) [see eq.(C·11) in Appendix C],

$$a_+ = b_+ = C_+ \exp \gamma t \quad \text{with} \quad a_- = b_- = c = 0 \,. \tag{3.10}$$

The rapid oscillation observed in Fig.5 is also elucidated by the linear analysis of eq.(3.10).

The exponentially growing solution in eqs.(3.10) and (C·11) is stabilized by applying the external shear flow potential of $|\Phi| > \gamma/2k^2$. Then one finds periodic solutions given by eqs.(C·14) and (C·15). For the benchmark test with a finite value of Φ, we employ the initial condition of

$$\begin{aligned} f_+(v) &= a_+(t=0) f_{Lr}(v) + b_+(t=0) f_{Li}(v) \\ f_-(v) &= a_-(t=0) f_{Lr}(v) + b_-(t=0) f_{Li}(v) \\ f_2(v) &= ic(t=0) f_{Li}(v), \end{aligned} \tag{3.11}$$

where $a_+(t=0) = -b_+(t=0) = 1$, $a_-(t=0) = b_-(t=0) = 1$, and $c(t=0) = 2\Phi$. The initial condition satisfies eq.(C·14) with $A_1 = A_2 = 1$. Here, $\Phi = 4.2$, which satisfies the stable condition of $\Phi > \gamma/2k^2 \simeq 4.16$. The other parameters are the same as in Fig.2. The implicit midpoint rule is used for the time-integration. We confirmed that the form of the three-mode solution in eq.(A·11) with $a_+(t) = -b_+(t)$, $a_-(t) = b_-(t)$, $c(t) = 2\Phi$ was conserved throughout the simulation. In Fig.6, one Finds that the simulation result (circular marks) agrees well with the elliptic orbit given by eq.(C·14). The observed period of $T = 517.25$ is very close to the theoretical value of $T = 2\pi/\Omega_0 = 518.6$.

§4. Benchmark tests for ITG turbulence

In this section, we describe results of benchmark tests for the ITG turbulence in the two-dimensional slab configuration which is the same as in the three-mode case but with many-mode interactions. The governing equations considered here are derived from the gyrokinetic equations[22] by assuming $\tilde{f}_{\boldsymbol{k}}(v_\parallel, v_\perp) = \tilde{f}_{\boldsymbol{k}}(v_\parallel) F_M(v_\perp)$. They are written in the wave number space such as

$$\partial_t \tilde{f}_{\boldsymbol{k}} + i\Theta v_\parallel k_y \tilde{f}_{\boldsymbol{k}} + \sum_{\boldsymbol{k}=\boldsymbol{k}'+\boldsymbol{k}''} \left(k'_y k''_x - k'_x k''_y\right) \Psi_{\boldsymbol{k}'} \tilde{f}_{\boldsymbol{k}''} =$$

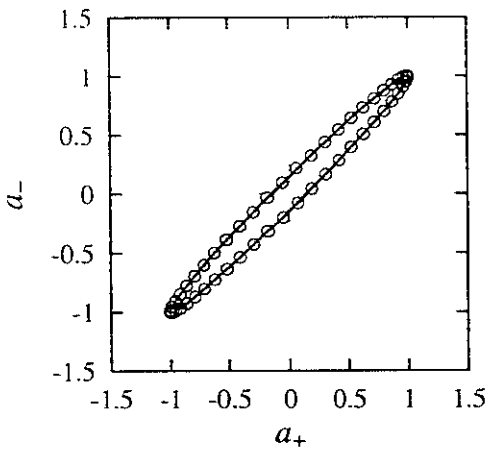

Fig. 6 Orbit in the (a_+, a_-)-phase space for $\Phi = 4.2$ with $b_+ = -a_+$, $b_- = a_-$, and $c = 2\Phi$. Solid line represents the analytical solution in eq.(C·14) with $A_1 = A_2 = 1$. Marks denote the simulation results plotted with a constant time interval of 40. Other parameters are the same as in Fig.2.

$$-ik_y\Psi_{\boldsymbol{k}}\left[1+(v_\parallel^2-1-k^2)\eta_i/2+\Theta v_\parallel\right]F_M(v_\parallel)\ , \quad (4.1)$$

$$\Psi_{\boldsymbol{k}} = e^{-k^2/2}\phi_{\boldsymbol{k}}\ , \quad (4.2)$$

and

$$\left[1-\Gamma_0(k^2)\right]\phi_{\boldsymbol{k}} = e^{-k^2/2}\int \tilde{f}_{\boldsymbol{k}}(v_\parallel)dv_\parallel - \tilde{n}_{e,\boldsymbol{k}}\ , \quad (4.3)$$

where $k^2 = k_x^2+k_y^2$, and $\Gamma_0(k^2) = \exp(-k^2)I_0(k^2)$. $I_0(z)$ means the 0-th modified Bessel function of z. The assumed Maxwellian in the perpendicular velocity would be valid, if a dominant wave length is much longer than the ion gyroradius. We also assume the adiabatic electron response as

$$\tilde{n}_{e,\boldsymbol{k}} = \begin{cases} \phi_{\boldsymbol{k}} & \text{for } k_y \neq 0 \\ 0 & \text{for } k_y = 0\ . \end{cases} \quad (4.4)$$

In our simulation code for the ITG turbulence, the convolution sum in eq.(4.1) is calculated in the real space by using the Fast Fourier Transform where the 3/2-rule is applied for de-aliasing, and then, is transformed back into the wave number space.

In the followings, we note the so-called entropy balance[7,20] which describes a relation between the entropy production rate and the transport flux. From eqs.(4.1)-(4.4), under the periodic boundary conditions in the x and y directions, one finds

$$\frac{d}{dt}(\delta S + W) = \eta_i Q_i \quad (4.5)$$

where

$$\delta S = \sum_{\boldsymbol{k}}\int dv_\parallel \frac{\left|\tilde{f}_{\boldsymbol{k}}\right|^2}{2F_M(v_\parallel)}\ ,$$

$$Q_i = \frac{1}{2}\sum_{\boldsymbol{k}}\int dv_\parallel\left(-ik_y e^{-k^2/2}\phi_{\boldsymbol{k}}\right)v_\parallel^2\tilde{f}_{-\boldsymbol{k}}\ ,$$

$$W = \frac{1}{2}\sum_{\boldsymbol{k}}\left(2-\Gamma_0(k^2)-\delta_{k_y,0}\right)|\phi_{\boldsymbol{k}}|^2\ . \quad (4.6)$$

Here, the definition of δS has the opposite sign as that in ref.20. Equation (4.5) tells us that no transport is observed ($Q_i = 0$) in a steady state of $d/dt(\delta S + W) = 0$. As discussed in §2.2, for a homogeneous version of eq.(4.1) where the right hand side vanishes, the implicit midpoint scheme guarantees the entropy conservation $[d(\delta S)/dt = 0]$. Thus, it is expected that our nondissipative simulation of eq.(4.1) accurately satisfies the balance equation, eq.(4.5).

Simulation parameters used here are given as follows; the maximum wave number $k_{x,\max} = k_{y,\max} = 3.2$, the interval in the wave number space $\Delta k = 0.05$ (thus, $\pm 64 \times \pm 64$ modes are included), $\Theta = 2.5$, $\eta_i = 10$, $-5v_t \leq v_\parallel \leq 5v_t$ and $\Delta t = 0.0125$. The normalization is the same as that in the three-mode problems. Amplitudes of $k_x = 0$ modes are fixed to zero, since the background density and temperature gradients are set to be constant in the x-direction. A convergence check for the grid spacing in $v_\parallel$ is carried out for $\Delta v_\parallel = 5v_t/16$, $5v_t/64$, $5v_t/256$, and $5v_t/1024$.

Time histories of $\eta_i Q_i$ and a residual $\Delta \equiv d(\delta S + W)/dt - \eta_i Q_i$ for the highest resolution of $\Delta v_\parallel = 5v_t/1024$ are plotted in Fig.7. Here, we employed the implicit midpoint scheme in eq.(2.14) for the time-integration. In this simulation, the shear (zonal) flow with $k_y = 0$ is excited after the linear growth of the

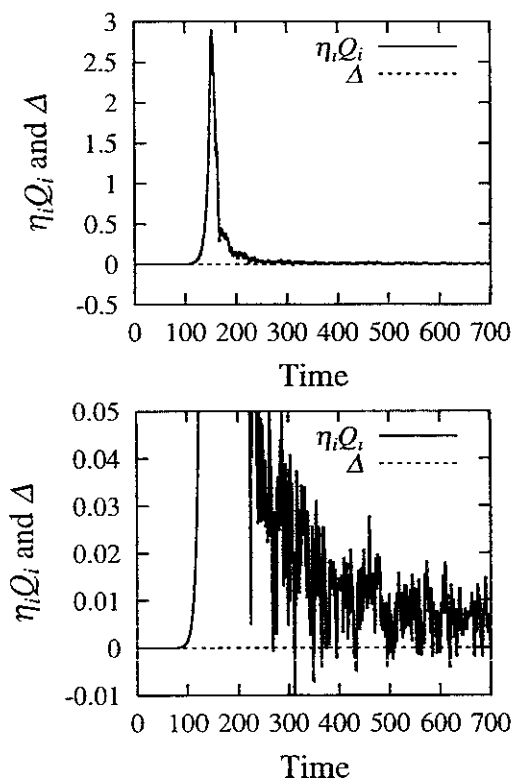

Fig. 7 Time-history of the thermal flux $\eta_i Q_i$ and the residual of the entropy balance Δ resulting from the nondissipative simulation of the ITG turbulence. The vertical axis of the upper panel is magnified in the lower.

ITG modes. The transport flux Q_i decreases after the peaking of $t \simeq 150$. This is because suppression of turbulence by the zonal flow leads to significant reduction of the transport flux. Then, we can see in the lower panel of Fig.7 that the flux reaches to a saturation level of $\eta_i Q_i \simeq 6.6 \times 10^{-3}$ (which corresponds to the ion thermal diffusivity of $\chi_i = Q_i/\eta_i = 6.6 \times 10^{-5}$ in the gyro-Bohm units). Throughout the simulation, the entropy balance in eq.(4.5) is well satisfied ($|\Delta| \ll |\eta_i Q_i|$). For comparison, we have also carried out the same simulation but with the predictor-corrector method for the time-integration, of which δS is shown in Fig.8 as a function of the time. In contrast to the case of the implicit mid-

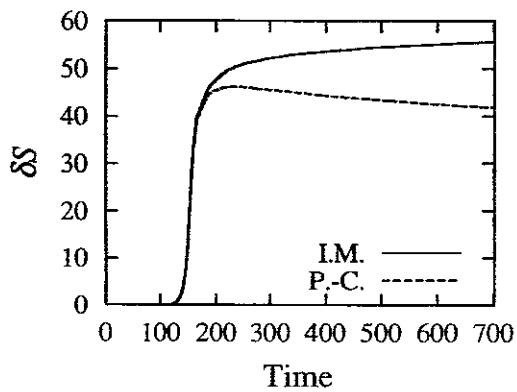

Fig. 8. Time-history of the entropy δS obtained by the nondissipative (implicit midpoint labeled as I.M.) and the dissipative (predictor-corrector labeled as P.-C.) simulations of the ITG turbulence.

point rule, δS decreases after the initial growth in the predictor-corrector simulation, although time-evolution of Q_i (not shown here) is almost the same as in Fig.7. Thus, the numerical dissipation inherent in the predictor-corrector method breaks the entropy balance ($\Delta < 0$).

In the simulations shown above, the transport flux Q_i saturates at a certain level in later time (roughly, $t \sim 500$ in Fig.7). The convergence check for $\Delta v_\parallel$ clarifies that, for coarser grid spacing in $v_\parallel$, saturation of Q_i is found at a higher level in earlier time. The saturated flux for different $\Delta v_\parallel$ is summarized in Fig.9, which shows a dependence of Q_i on a power of $\Delta v_\parallel$ (that is, $Q_i \propto (\Delta v_\parallel)^{-\beta}$ with $\beta \simeq 0.85$). Here, the error bars are calculated by the root-mean-square of fluctuations of $\eta_i Q_i$. Thus, it is considered that the flux vanishes when $\Delta v_\parallel \to 0$. The observed saturation is, therefore, artificial due to discreteness of the grids in the velocity space. The reason is considered as follows. Suppose a fluctuation is given in a collisionless electrostatic plasma. Then, the phase mixing generates finer fluctuations in the velocity space such as the ballistic mode. After the fluctuation scale-length in the velocity space becomes comparable to $\Delta v_\parallel$ (it is found at $t \simeq 250$ in the simulation in Fig.7), an aliasing error arises. The aliasing error affects the density and electric field calculations, and leads to the continuous increase of δS that balances with the artificial transport flux. This is equivalent to a phenomenon so called recurrence[14] in the Vlasov simulations. There-

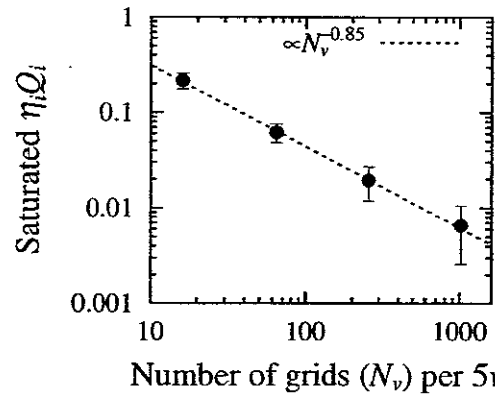

Fig. 9. A convergence check for the velocity space resolution (grid numbers per $5v_t$) in terms of the saturated thermal flux $\eta_i Q_i$.

fore, the collisionless simulation considered here is valid only in a finite time period when the fluctuation scale is well resolved in the velocity space.

§5. Summary

We have carried out the comprehensive benchmark tests of our newly developed simulation code with the nondissipative time-integration scheme such as the implicit midpoint rule. In order to establish a reliable reference for simulations of the ITG turbulence, we have derived the asymmetric three-mode ITG equations, and have found a special class of the solutions with a constant $(2, 0)$ mode. The dissipative three-mode equations with the Krook collision term are also given with the stationary solutions. The simulation results of the asymmetric and the dissipative three-mode ITG problems agree with the theoretical analyses. It is also confirmed that the nondissipative simulation more correctly reproduces the periodic solution of the collisionless three-mode problem than the predictor-corrector and the Runge-Kutta-Gill methods. Then, the simulation code is extended to include many-mode interactions through the $E \times B$ nonlinearity. The nondissipative simulation results of the slab ITG turbulence accurately satisfy the balance equation between the entropy production rate, the temporal change of the potential energy and the ion thermal flux, while the predictor-corrector scheme fails to balance them due to the numerical dissipation. The benchmark test for the ITG turbulence also raises a critical issue of collisionless turbulence simulations. Under the parameters and the model settings employed in the present simulations, the saturation level of the thermal flux has a power-law scaling on the velocity space resolution. This means that the observed saturation is artificial due to the aliasing error in the velocity space. Since the phase mixing generates finer fluctuations, in a strict sense, the collisionless simulation of the ITG turbulence is possible within a finite time period. This problem will be pursued in detail elsewhere by means of the nondissipative simulations developed here with a higher velocity space resolution.

Acknowledgments

One of the authors (T.-H.W.) would like to thank Dr Y Todo and Dr.C.Bolton for their fruitful comments and discussions. Numerical computations in this study are performed on the NIFS MISSION System (Man-Machine Interactive System for Simulation). This work is supported in part by the Grant-in-Aid from the Japanese Ministry of Education, Culture, Sports, Science and Technology, No.12680497.

Appendix A: Asymmetric three-mode ITG equations

From eqs.(3.1) and (3.2), the asymmetric three-mode ITG equations are given by

$$(\partial_t + ik\Theta v)f_+(v,t) + 2k^2\left[\phi_-(t)f_2(v,t) - \phi_2(t)f_-(v,t)\right] = -ik\phi_+(t)G(v)\ , \tag{A·1}$$

$$(\partial_t + ik\Theta v)f_-(v,t) + 2k^2\left[-\phi_+(t)f_2^*(v,t) + \phi_2^*(t)f_+(v,t)\right] = -ik\phi_-(t)G(v)\ , \tag{A·2}$$

$$\partial_t f_2(v,t) = 2k^2\left[\phi_-^*(t)f_+(v,t) - \phi_+(t)f_-^*(v,t)\right]\ , \tag{A·3}$$

$$\phi_+(t) = \int dv\ f_+(v,t)\ , \tag{A·4}$$

$$\phi_-(t) = \int dv\ f_-(v,t)\ , \tag{A·5}$$

and

$$\int dv\ f_2(v,t) = 0\ , \tag{A·6}$$

where the subscripts $+$, $-$, and 2 mean the $(1,1)$, $(-1,1)$, and $(2,0)$ modes, respectively. In the drift kinetic limit with the adiabatic electrons, however, there is no adequate equation describing $\langle\phi\rangle$ ($=\phi_2$ in the three-mode case) which accounts for the mean shear flow. In this analysis, therefore, ϕ_2 is regarded as an externally-given function of the time t, while it is fixed to zero in the symmetric three-mode equations.[6] $G(v)$ is defined as

$$G(v) \equiv \left[1 + \frac{\eta_i}{2}(v^2-1) + \Theta v\right]F_M(v)\ . \tag{A·7}$$

Requiring $f_+ = f_-$, $\mathrm{Re}[f_2] = 0$, $\phi_+ = \phi_-$, and $\phi_2 = 0$ in eqs.(A·1)-(A·6), one finds the symmetric three-mode equations.

The linearized version of the three-mode equations with $\phi_2 = 0$ has a linear solution of the form

$$[f_+(v,t), f_-(v,t), f_2(v,t), \phi_+(t), \phi_-(t)] = [f_L(v), f_L(v), h_L(v), \phi_L, \phi_L]\exp(-i\omega t)\ .$$

Here, the linear eigenfunctions are given by

$$\begin{aligned} f_L(v) &\equiv f_{Lr}(v) + if_{Li}(v) \\ &\equiv \frac{kG(v)}{(\omega_r - k\Theta v) + i\gamma} \\ &\equiv \frac{kG(v)[(\omega_r - k\Theta v) - i\gamma]}{(\omega_r - k\Theta v)^2 + \gamma^2}\ , \end{aligned} \tag{A·8}$$

$$h_L(v) \equiv 0, \quad \text{and} \quad \phi_L \equiv 1 \quad \text{(normalization)}\ , \tag{A·9}$$

and the complex eigenfrequency $\omega = \omega_r + i\gamma$ is determined by the dispersion relation

$$\int dv\ f_L(v) \equiv \int dv \frac{kG(v)}{(\omega_r - k\Theta v) + i\gamma} = 1\ , \tag{A·10}$$

where $\gamma > 0$ is assumed.

Hereafter, we consider the case of $\phi_2(t) = \Phi$ where Φ is a real-valued constant. Thus, in the same way as in the symmetric case, eqs.(A·1)–(A·6) have a class of exact solutions which are written in terms of the real and imaginary parts of the eigenfunction $f_L(v)$ and the real eigenfrequency ω_r as

$$\begin{aligned} f_+(v,t) &= [a_+(t)f_{Lr}(v) + ib_+(t)f_{Li}(v)]\exp(-i\omega_r t), \\ f_-(v,t) &= [a_-(t)f_{Lr}(v) + ib_-(t)f_{Li}(v)]\exp(-i\omega_r t), \\ f_2(v,t) &= ic(t)f_{Li}(v), \\ \phi_+(t) &= a_+(t)\exp(-i\omega_r t)\ , \\ \phi_-(t) &= a_-(t)\exp(-i\omega_r t)\ , \end{aligned} \tag{A·11}$$

where $a_+(t)$, $a_-(t)$, $b_+(t)$, $b_-(t)$ and $c(t)$ are real-valued functions of the time t. Equation (A·11) automatically satisfies eqs.(A·4)–(A·6). Substituting these into eqs.(A·1)–(A·3) and using eq.(A·8), we obtain a set of ordinary differential equations for $[a_+(t), a_-(t), b_+(t), b_-(t), c(t)]$,

$$\begin{aligned} da_+/dt &= \gamma b_+ + 2k^2\Phi a_-\ , \\ da_-/dt &= \gamma b_- - 2k^2\Phi a_+\ , \\ db_+/dt &= \gamma a_+ + 2k^2\Phi b_- - 2k^2 a_- c\ , \\ db_-/dt &= \gamma a_- - 2k^2\Phi b_+ - 2k^2 a_+ c\ , \\ dc/dt &= 2k^2\left(a_+ b_- + a_- b_+\right). \end{aligned} \tag{A·12}$$

The above equations involve the set of ordinary differential equations for the symmetric case [eq.(15) in ref.6] as a subset with $a_+ = a_-$, $b_+ = b_-$, and $\Phi = 0$.

Appendix B: Symmetric three-mode equations with Krook collision term

Adding the Krook collision term $-\nu\tilde{f}$ to the right hand side of eq.(3.1), after manipulation similar to Appendix A, one finds that the dissipative three-mode ITG equations have the same type of exact solutions as the nondissipative one in eq.(3.5). In the presence of the Krook collision term, $a(t)$, $b(t)$, and $c(t)$ are given by the ordinary differential equations,

$$\begin{aligned} da/dt &= \gamma b - \nu a\ , \\ db/dt &= \gamma a - 2k^2 ac - \nu b\ , \\ dc/dt &= 4k^2 ab - \nu c. \end{aligned} \tag{B·1}$$

Here, γ means the growth rate for $\nu = 0$. The linear growth rate with the Krook collision term is $\gamma - \nu$. Equation (B·1) has a trivial exact solution,

$$(a,b,c) = \left(0, 0, c_s e^{-\nu t}\right)\ , \tag{B·2}$$

with an arbitrary constant c_s. When we consider time-evolutions of the unstable modes ($\gamma > \nu$) which linearly grow from small initial perturbations, it is more important to note that eq.(B·1) is non-conservative, and that there are stable stationary points of

$$(a,b,c) = \left(\pm\frac{\sqrt{\gamma^2-\nu^2}}{2\sqrt{2}k^2}, \pm\frac{\nu\sqrt{\gamma^2-\nu^2}}{2\sqrt{2}k^2\gamma}, \frac{\gamma^2-\nu^2}{2k^2\gamma} \right) . \tag{B·3}$$

In the limit of $\nu \to 0$, the stationary points of eq.(B·3) are located on the center of periodic orbits given by the nondissipative symmetric three-mode equation [eq.(16) in ref.6]. Thus, following a spiral orbit after the linear growth, the solution of eq.(B·1) approaches to one of the stable stationary points of eq.(B·3).

Appendix C: Fundamental properties of eq. (A·12)

C.1 Invariance and conservation property

Here, we consider some fundamental properties of the set of ordinary differential equations, eq.(A·12), derived from the asymmetric three-mode equations. Equation (A·12) is invariant to the following transforms,

$$\begin{aligned} &(a_+,a_-,b_+,b_-,c,\Phi) \to (-a_+,-a_-,-b_+,-b_-,c,\Phi) , \\ &(a_+,a_-,b_+,b_-,c,\Phi) \to (-a_+,a_-,-b_+,b_-,-c,-\Phi) , \\ &(a_+,a_-,b_+,b_-,c,\Phi) \to (a_+,-a_-,b_+,-b_-,-c,-\Phi) . \end{aligned} \tag{C·1}$$

When we rewrite eq.(A·12) as $d\boldsymbol{\xi}/dt = \boldsymbol{F}(\boldsymbol{\xi})$ for $\boldsymbol{\xi} \equiv (a_+,a_-,b_+,b_-,c)^t$, $\nabla \cdot \boldsymbol{F}(\boldsymbol{\xi}) = 0$ (there is no sink and source of the flow $\boldsymbol{F}$ in the $\boldsymbol{\xi}$-space). Thus, eq.(A·12) is conservative.

From eq.(A·12) for any value of Φ, we easily find

$$a_+^2 + a_-^2 - b_+^2 - b_-^2 - c^2 = C_0 , \tag{C·2}$$

where C_0 is a constant. For $\Phi = 0$ with no shear flow, furthermore, eq.(A·12) has the another constant of motion, C_1,

$$c - \frac{2k^2}{\gamma} a_+ a_- = C_1 , \tag{C·3}$$

which corresponds to eq.(20) in ref.6. Eliminating c from eq.(A·12) by using eq.(C·3), one finds that eq.(A·12) can be written in a Hamiltonian form,

$$\frac{d\boldsymbol{\zeta}}{dt} = \mathsf{J}\frac{\partial H}{\partial \boldsymbol{\zeta}}$$

where $\boldsymbol{\zeta} \equiv (a_+,a_-,b_+,b_-)^t$ and

$$H(a_+,a_-,b_+,b_-) = \frac{\gamma}{2}\left(b_+^2 + b_-^2 - a_+^2 - a_-^2\right) + 2k^2 C_1 a_+ a_- + \frac{2k^4}{\gamma} a_+^2 a_-^2 , \tag{C·4}$$

with

$$\mathsf{J} = \begin{pmatrix} \mathsf{O} & \mathsf{I} \\ -\mathsf{I} & \mathsf{O} \end{pmatrix} .$$

O and I are the zero and unit matrices of 2×2. A similar Hamiltonian form is also derived for the symmetric case.[7)]

C.2 Stationary solutions

For any Φ, eq.(A·12) has two types of stationary solutions, trivial and nontrivial ones, which are written as

$$(a_+,a_-,b_+,b_-,c) = (0,0,0,0,c_s) , \tag{C·5}$$

$$(a_+,a_-,b_+,b_-,c) = \left[a_s, a_s, -\frac{2k^2\Phi}{\gamma}a_s, \frac{2k^2\Phi}{\gamma}a_s, \frac{\gamma}{2k^2}\left(1+\frac{4k^4\Phi^2}{\gamma^2}\right) \right] , \tag{C·6}$$

and

$$(a_+,a_-,b_+,b_-,c) = \left[a_s, -a_s, \frac{2k^2\Phi}{\gamma}a_s, \frac{2k^2\Phi}{\gamma}a_s, -\frac{\gamma}{2k^2}\left(1+\frac{4k^4\Phi^2}{\gamma^2}\right) \right] , \tag{C·7}$$

where a_s and c_s are arbitrary constants. When $\Phi = 0$, the solution in eq.(C·6) coincides with the stationary solution of the symmetric case [eq.(16) in ref.6].

Let us consider the linear stability of the stationary solutions. For the trivial solution in eq.(C·5), the linear stability analysis gives complex eigenvalues Ω and eigenfunctions $\exp(\Omega t)$, where

$$\Omega^2 = \gamma^2 - 4k^4\Phi^2 \pm i2k^2\gamma\sqrt{4\Phi^2 - c_s^2} . \tag{C·8}$$

Only if

$$|\Phi| > \gamma/2k^2 \quad \text{and} \quad 2|\Phi| < |c_s| < \frac{\gamma}{2k^2}\left(\frac{4k^4\Phi^2}{\gamma^2}+1\right) , \tag{C·9}$$

one finds pure imaginary roots of eq.(C·8). Otherwise, the solution in eq.(C·5) consists of unstable stationary points. For $\Phi = 0$ and $c_s = 0$, $\Omega = \pm\gamma$ which corresponds to linear eigenvalues on the separatrix point found in the symmetric three-mode coupling system.[6)] From the linear analysis for eqs.(C·6) and (C·7), one finds complex or pure imaginary roots depending on $|\Phi|$,

$$\Omega = \pm\sqrt{2(\gamma^2 - 4k^4\Phi^2)} \equiv \sqrt{2}\Omega_0 , \tag{C·10}$$

as well as two other pure imaginary ones, $\Omega = \pm i2\sqrt{2}k^2\Phi$.

C.3 Nonstationary solutions

In addition to the symmetric exact solution which was studied in detail in ref.6, there are a different type of exact analytical solutions of eq.(A·12) with $dc/dt = 0$.

For $\Phi = 0$, eq.(A·12) has a stable/unstable solution given by

$$\begin{aligned} a_+ &= C_+ e^{\gamma t} + D_+ e^{-\gamma t}, \\ a_- &= C_- e^{\gamma t} + D_- e^{-\gamma t}, \\ b_+ &= C_+ e^{\gamma t} - D_+ e^{-\gamma t}, \\ b_- &= C_- e^{\gamma t} - D_- e^{-\gamma t}, \\ c &= 0 , \end{aligned} \tag{C·11}$$

where $C_+C_- = 0$ and $D_+D_- = 0$.

By substituting $b_+ = -a_+$, $b_- = a_-$, and $c = 2\Phi$ into eq.(A·12), which satisfy $dc/dt = 0$, one finds that the above solution is extended to a case of $\Phi \neq 0$. Then, one obtains

$$a_+ + a_- = \mathrm{Re}\left(A_1\epsilon^{\Omega_0 t} + A_2\epsilon^{-\Omega_0 t}\right) ,$$
$$a_+ - a_- = -\frac{1}{\gamma + 2k^2\Phi}\mathrm{Re}\left(\Omega_0\left[A_1\epsilon^{\Omega_0 t} - A_2\epsilon^{-\Omega_0 t}\right]\right) , \tag{C·12}$$

where $\Omega_0 = \pm\sqrt{\gamma^2 - 4k^4\Phi^2}$ [this is identical to Ω_0 defined in eq.(C·10)]. For $b_+ = a_+$, $b_- = -a_-$, and $c = -2\Phi$, the another exact solution of eq.(A·12) is derived, that is,

$$a_+ + a_- = \mathrm{Re}\left(A_3\epsilon^{\Omega_0 t} + A_4\epsilon^{-\Omega_0 t}\right) ,$$
$$a_+ - a_- = \frac{1}{\gamma - 2k^2\Phi}\mathrm{Re}\left(\Omega_0\left[A_3\epsilon^{\Omega_0 t} - A_4\epsilon^{-\Omega_0 t}\right]\right) . \tag{C·13}$$

Here, A_n $(n = 1, 2, 3, 4)$ denote arbitrary constants. As seen in the definition of Ω_0, when $|\Phi|$ exceeds $\gamma/2k^2$, unstable orbits of eqs.(C·12) and (C·13) change to periodic (elliptic) ones which are, respectively, given by

$$(2k^2\Phi - \gamma)(a_+ + a_-)^2 + (2k^2\Phi + \gamma)(a_+ - a_-)^2 = (2k^2\Phi - \gamma)(A_1 + A_2)^2 \tag{C·14}$$

for $b_+ = -a_+$, $b_- = a_-$, $c = 2\Phi$, and

$$(2k^2\Phi + \gamma)(a_+ + a_-)^2 + (2k^2\Phi - \gamma)(a_+ - a_-)^2 = (2k^2\Phi + \gamma)(A_3 + A_4)^2 \tag{C·15}$$

for $b_+ = a_+$, $b_- = -a_-$, $c = -2\Phi$, where A_n are real-valued.

Appendix D: Linear stability analysis of eq. (3.10)

Linearizing eq.(A·12) around the exponentially growing solution in eq.(3.10) [or eq.(C·11) in Appendix C with $C_- = D_+ = D_- = 0$] with perturbations of $|\tilde{a}_-|, |\tilde{b}_-|, |\tilde{c}| \ll |a_+|, |b_+|$, one finds

$$d\tilde{a}_-/dt = \gamma\tilde{b}_- ,$$
$$d\tilde{b}_-/dt = \gamma\tilde{a}_- - 2k^2C_+e^{\gamma t}\tilde{c} ,$$
$$d\tilde{c}/dt = 2k^2C_+e^{\gamma t}(\tilde{a}_- + \tilde{b}_-) . \tag{D·1}$$

A general solution of eq.(D·1) is given by

$$\tilde{a}_-(t) = \frac{\gamma}{2k^2C_+}\left[\, B_1J_1\left(2k^2|C_+|e^{\gamma t}/\gamma\right) + B_2N_1\left(2k^2|C_+|e^{\gamma t}/\gamma\right)\right] + B_3e^{-\gamma t}, \tag{D·2}$$

$$\tilde{b}_-(t) - \frac{C_+}{2|C_+|}e^{\gamma t}\left\{\, B_1\left[J_0\left(2k^2|C_+|e^{\gamma t}/\gamma\right) - J_2\left(2k^2|C_+|e^{\gamma t}/\gamma\right)\right] + B_2\left[N_0\left(2k^2|C_+|e^{\gamma t}/\gamma\right) - N_2\left(2k^2|C_+|e^{\gamma t}/\gamma\right)\right]\right\} - B_3e^{-\gamma t} \tag{D·3}$$

and

$$\tilde{c}(t) = \epsilon^{\gamma t}\left[B_1J_1\left(2k^2|C_+|\epsilon^{\gamma t}/\gamma\right) + B_2N_1\left(2k^2|C_+|\epsilon^{\gamma t}/\gamma\right)\right] . \tag{D·4}$$

where B_1, B_2, and B_3 are arbitrary constants. $J_n(z)$ and $N_n(z)$ denote the n-th Bessel functions of the first and second kinds, respectively

Using the asymptotic expansion of the Bessel functions for large z, $J_n(z) \sim \sqrt{2/\pi z}\cos[z - (2n+1)\pi/4]$ and $N_n(z) \sim \sqrt{2/\pi z}\sin[z - (2n+1)\pi/4]$, the oscillation amplitudes of $\tilde{a}_-$, $\tilde{b}_-$, and $\tilde{c}$ are estimated as $|\tilde{a}_-(t)| \sim \exp(-\gamma t/2)$, $|\tilde{b}_-(t)| \sim \exp(\gamma t/2)$, and $|\tilde{c}(t)| \sim \exp(\gamma t/2)$, respectively On the other hand, since $a_+ = b_+ \propto \exp(\gamma t)$, $|\tilde{a}_-/a_+|$, $|\tilde{b}_-/a_+|$, and $|\tilde{c}/a_+|$ exponentially decrease for the time t. This means that the linear approximation in eq.(D·1) continues to be valid or, say, becomes better as t increases. Thus, a_+ and b_+ continue to grow exponentially with the rate of γ, when the initial point of (a_+, a_-, b_+, b_-, c) is located in the vicinity of the exact solution in eq.(3.10) Amplitudes of b_- and c also show the exponential growth but with the smaller rate of $\gamma/2$, while a_- (and hence $|\phi_-|$) decreases with a damping rate of $\gamma/2$. The same argument can be applied to the case of $C_+ = 0$ but $C_- \neq 0$ Therefore, one expects a predominant growth of one mode after the symmetry breaking given by eq (3.8). This is consistent with the simulation result in Fig.5. In addition, as t increases, distances between zero points of $\tilde{a}_-(t)$, $\tilde{b}_-(t)$, $\tilde{c}(t)$ exponentially decrease, which explains the rapid oscillation of $(-1, 1)$ mode in Fig.5.

1) W. Horton: Rev. Mod. Phys. **71** (1999) 735
2) W. W Lee and W. M. Tang· Phys. Fluids **31** (1988) 612.
3) L. I. Rudakov and R Z. Sagdeev Dokl Akad. Nauk SSSR **138** (1961) 581 [English transl.. Soviet Phys. Dokl. **6** (1961) 415]
4) S. E. Parker, W Dorland, R. A. Santoro, M. A. Beer, Q P. Liu, W W. Lee, and G. W. Hammett. Phys. Plasmas **1** (1994) 1461.
5) N Mattor and S. E Parker· Phys. Rev Lett **79** (1997) 3419.
6) T.-H. Watanabe, H. Sugama, and T Sato: Phys Plasmas **7** (2000) 984.
7) H Sugama, T -H Watanabe, and W Horton· Phys Plasmas **8** (2001) 2617.
8) J F Federici, W. W. Lee, and W M. Tang: Phys Fluids **30** (1987) 425
9) A M Dimits· Phys. Fluids B **2** (1990) 1768
10) W. W. Lee and H. Okuda. J Compt Phys. **26** (1978) 139.
11) T. Tajima: *Computational Plasma Physics: With Applications to Fusion and Astrophysics* (Addison-Wesley, Redwood City, CA, 1989) p.194.
12) Z Lin, T S Hahm W. W Lee W M Tang, and R. B. White: Science **281** (1998) 1835.
13) Z. Lin, T S Hahm, W W Lee, W. M Tang, and P. H Diamond. Phys. Rev. Lett. **83** (1999) 3645
14) C. Z. Cheng and G. Knorr J Compt Phys **22** (1976) 330
15) E. Forest and R D Ruth Physica D **43** (1990) 105.
16) H Yoshida Phys Lett A **150** (1990) 262
17) A Ghizzo, B Izrar, P Bertrand, E. Fijalkow, M R Feix, and M. Shoucri: Phys Fluids **31** (1988) 72.
18) C. K. Birdsall and A B. Langdon. *Plasma Physics via Computer Simulation* (McGraw-Hill, New York, 1985)
19) J. M Sanz-Serna Physica D **60** (1992) 293
20) J. A Krommes and G Hu Phys Plasmas **1** (1994) 3211.
21) J deFrutos and J M. Sanz-Serna. J Comput Phys. **103** (1992) 160
22) D. H E. Dubin, J. A Krommes, C. Oberman, and W W Lee Phys Fluids **26** (1983) 3524

Recent Issues of NIFS Series

NIFS-681 Alexander A Shishkin
Estafette of Drift Resonances Stochasticity and Control of Particle Motion in a Toroidal Magnetic Trap Feb 2001

NIFS-682 H Momota and G H Miley
Virtual Cathode in a Spherical Inertial Electrostatic Confinement Device Feb 2001

NIFS-683 K Saito, R Kumazawa, T Mutoh T Seki T Watari, Y Torii, D A Hartmann, Y Zhao A Fukuyama F Shimpo, G Nomura M Yokota, M Sasao, M Isobe M Osakabe T Ozaki K Narihara, Y Nagayama, S Inagaki, K Itoh, S Morita, A V Krasilnikov K Ohkubo M Sato, S Kubo T Shimozuma, H Idei, Y Yoshimura O Kaneko, Y Takeiri, Y Oka, K Tsumori, K Ikeda, A Komori H Yamada, H Funaba, K Y Watanabe, S Sakakibara, M Shoji, R Sakamoto, J Miyazawa, K Tanaka, B J Peterson, N Ashikawa S Murakami, T Minami, S Ohakachi S Yamamoto, S Kado H Sasao, H Suzuki, K Kawahata, P deVries, M Emoto, H Nakanishi T Kobuchi N Inoue, N Ohyabu, Y Nakamura, S Masuzaki S Muto, K Sato, T Morisaki, M Yokoyama, T Watanabe, M Goto I Yamada, K Ida T Tokuzawa, , N Noda, S Yamaguchi, K Akaishi, A Sagara, K Toi K Nishimura, K Yamazaki, S Sudo Y Hamada, O Motojima, M Fujiwara,
Ion and Electron Heating in ICRF Heating Experiments on LHD Mar 2001

NIFS-684 S Kida and S Goto,
Line Statistics Stretching Rate of Passive Lines in Turbulence Mar 2001

NIFS-685 R Tanaka, T Nakamura and T Yabe,
Exactly Conservative Semi-Lagrangian Scheme (CIP-CSL) in One-Dimension Mar 2001

NIFS-686 S Toda and K Itoh,
Analysis of Structure and Transition of Radial Electric Field in Helical Systems Mar 2001

NIFS-687 T Kuroda and H Sugama,
Effects of Multiple-Helicity Fields on Ion Temperature Gradient Modes Apr 2001

NIFS-688 M. Tanaka,
The Origins of Electrical Resistivity in Magnetic Reconnection Studies by 2D and 3D Macro Particle Simulations Apr 2001

NIFS-689 A. Maluckov, N Nakajima, M Okamoto, S Murakami and R Kanno,
Statistical Properties of the Neoclassical Radial Diffusion in a Tokamak Equilibrium Apr 2001

NIFS-690 Y Matsumoto, T Nagaura, Y Itoh, S-I Oikawa and T Watanabe,
LHD Type Proton-Boron Reactor and the Control of its Peripheral Potential Structure Apr 2001

NIFS-691 A Yoshizawa, S -I Itoh, K Itoh and N Yokoi,
Turbulence Theories and Modelling of Fluids and Plasmas Apr 2001

NIFS-692 K. Ichiguchi, T Nishimura, N Nakajima, M Okamoto, S.-i Oikawa, M Itagaki,
Effects of Net Toroidal Current Profile on Mercier Criterion in Heliotron Plasma Apr 2001

NIFS-693 W Pei, R Horiuchi and T Sato,
Long Time Scale Evolution of Collisionless Driven Reconnection in a Two-Dimensional Open System Apr. 2001

NIFS-694 L N Vyachenslavov, K Tanaka, K Kawahata,
CO2 Laser Diagnostics for Measurements of the Plasma Density Profile and Plasma Density Fluctuations on LHD Apr 2001

NIFS-695 T Ohkawa,
Spin Dependent Transport in Magnetically Confined Plasma May 2001

NIFS-696 M Yokoyama, K Ida, H Sanuki, K Itoh, K Narihara, K Tanaka, K Kawahata, N Ohyabu and LHD experimental group
Analysis of Radial Electric Field in LHD towards Improved Confinement May 2001

NIFS-697 M. Yokoyama, K. Itoh S Okamura, K Matsuoka, S -I Itoh,
Maximum-J Capability in a Quasi-Axisymmetric Stellarator. May 2001

NIFS-698 S-I. Itoh and K Itoh,
Transition in Multiple-scale-lengths Turbulence in Plasmas May 2001

NIFS-699 K. Ohi, H Naitou, Y Tauchi, O Fukumasa,
Bifurcation in Asymmetric Plasma Divided by a Magnetic Filter May 2001

NIFS-700 H Miura, T Hayashi and T Sato,
Nonlinear Simulation of Resistive Ballooning Modes in Large Helical Device June 2001

NIFS-701 G Kawahara and S. Kida,
A Periodic Motion Embedded in Plane Couette Turbulence June 2001

NIFS-702 K Ohkubo,
Hybrid Modes in a Square Corrugated Waveguide June 2001

NIFS-703 S.-I Itoh and K Itoh,
Statistical Theory and Transition in Multiple-scale-lengths Turbulence in Plasmas June 2001

NIFS-704 S Toda and K Itoh,
Theoretical Study of Structure of Electric Field in Helical Toroidal Plasmas June 2001

NIFS-705 K Itoh and S-I Itoh,
Geometry Changes Transient Transport in Plasmas June 2001

NIFS-706 M Tanaka and A Yu Grosberg
Electrophoresis of Charge Inverted Macroion Complex Molecular Dynamics Study July 2001

NIFS-707 T-H Watanave, H Sugama and T Sato
A Nondissipative Simulation Method for the Drift Kinetic Equation, July 2001